Research Article | Vol. 29, No. 26 / 20 Dec 2021 / Optics Express 44174

Optics EXPRESS

Design of an X-cut thin-film lithium niobate waveguide as a passive polarization rotator

LUIS CORTES-HERRERA,[1,*] XIAOTONG HE,[1] JAIME CARDENAS,[1] AND GOVIND P. AGRAWAL[1]

[1]The Institute of Optics, University of Rochester, Rochester, New York 14627, USA
[*]lcortesh@ur.rochester.edu

Abstract: The transverse-electric and transverse-magnetic modes of an X-cut thin-film lithium niobate waveguide vary in effective indices and exchange power when the waveguide makes an oblique angle with its crystallographic Z-axis, i.e. its optics axis. We leverage this phenomenon to design a passive fundamental-mode polarization rotator. In our design, the lithium niobate waveguide is tilted at an optimum angle with respect to its Z-axis, such that material anisotropy induces phase-matched polarization conversion. We discuss the rotator's ideal-device length, crosstalk, and bandwidth. The proposed design yields compact (shorter than 1 mm), low-loss, passive polarization rotators for telecom wavelengths.

1. Introduction

Lithium-niobate-on-insulator (LNOI) waveguides, also known as thin-film lithium-niobate (LN) waveguides, have attracted considerable attention because of their excellent electro-optic properties [1–4]. In particular, they have been used to make microring resonators [3,5]. Recently, we developed a coupled-mode theory (CMT), describing coupling between the transverse-electric (TE) and transverse-magnetic (TM) modes when the LN core is either X-cut or Y-cut and its crystallographic Z-axis (i.e. its optic axis) makes an oblique angle with the etched waveguide [6]. In this paper, we utilize this theory to design a passive polarization rotator, which directly transfers power from its fundamental TE mode to its fundamental TM mode. Essentially, the rotator consists of an X-cut LNOI waveguide tilted at an optimum angle with respect to its Z-axis, such that the core's material anisotropy induces both polarization coupling and a vanishing modal birefringence, resulting in phase-matched polarization conversion.

The guided modes of anisotropic waveguides have been analyzed for decades [7–11]. In particular, the effect of LN's material birefringence on the polarization properties of X-cut LNOI waveguides has been the topic of several theoretical and experimental investigations [6,12–14]. It has also been utilized to design polarization-engineering devices such as TE/TM-pass polarizers [15,16], polarization beam splitters [17–19], and birefringence-free waveguides [20,21]. Polarization rotation via the electro-optic effect in LNOI [22] and via material anisotropy of oblique deposition of columnar thin films [23] have also been proposed. However, a design for a passive LNOI polarization rotator utilizing LN's material birefringence has yet to be presented. That is the objective of this paper.

The influence of LN's material birefringence on the polarization characteristics of guided modes has also been investigated for bulk titanium-indiffused lithium niobate (Ti:$LiNbO_3$) waveguides. In this context, slight off-Z-axis propagation was originally proposed [24] so material birefringence compensates for residual geometric birefringence in electro-optical polarization rotators. In that work, it was also identified that off-Z-axis propagation induces passive polarization coupling. Later, both the change in polarization effective indices and polarization coupling in off-Z-axis Ti:$LiNbO_3$ waveguides were analyzed [25–27] using CMT

#445412 https://doi.org/10.1364/OE.445412
Journal © 2021 Received 10 Oct 2021; revised 30 Nov 2021; accepted 3 Dec 2021; published 17 Dec 2021

Optics EXPRESS

[28]. A passive polarization rotator based on passive coupling in Ti:$LiNbO_3$ waveguides was even proposed and characterized through a vectorial beam propagation method [29].

However, the optical guiding properties of LNOI differ drastically from those of Ti:$LiNbO_3$, so polarization rotation in LNOI waveguides must be examined independently, as we do in this paper. This is because LNOI waveguides have an index contrast much larger than that of Ti:$LiNbO_3$ waveguides, roughly by an order of magnitude [5]. Consequently, LNOI waveguides possess much larger geometric birefringence, so polarization-mode phase-matching can be achieved at much greater deviations from the Z-axis. This, we find, results in correspondingly more efficient polarization rotation. Additionally, larger index contrast permits the etching of sharp waveguide bends [5]. This allows one to tightly delimit the polarization rotator length with such bends, as in our proposed design, depicted below.

The remainder of this paper is organized as follows. In Section 2., we describe the geometry of the proposed polarization rotator, and examine analytically its polarization properties via CMT. In Section 3., we evaluate the CMT design numerically and study the resulting characteristics of the polarization rotator such as device length, crosstalk, and bandwidth. In Section 4., we present our conclusions.

2. Proposed design and CMT analysis

2.1. Polarization rotator geometry

Our proposed design is shown in Figs. 1(a) and 1(b) in its two possible configurations. It consists of a LNOI waveguide with a tilted section of length L, joined at its two ends by untilted (or straight) segments. The direction of propagation along the tilted segment makes an oblique angle ϕ with that along the straight sections. Along the straight segments, the direction of propagation is parallel to either LN's Y-axis or Z-axis, depending on the chosen configuration. In Configuration Y (Fig. 1), the direction of propagation is parallel to the Y-axis. In Configuration Z (Fig. 1(b)), it is parallel to the Z-axis. The CMT of polarization coupling in Sections 2.2 and 2.3 applies equally well to both configurations. The differences in performance between both configurations are few and are summarized in Sections 2.4 and 3.3.

In practice, each joint consist of a circular arc, as shown for the first joint in Fig. 1(c). The second joint is bent similarly to the first. Note that the deviation angle ϕ is equal to the angle spanned by the curved segment with radius of curvature r. Naturally, the radii of curvature r must be large enough to avoid noticeable bending losses. In our analytical design, we assume that the radii are still small enough so polarization coupling in each of the circular joints is negligible. However, the finite curvature of these joints induces residual crosstalk. In Section 2.3, we provide a perturbative expression and a simple bound for this residual crosstalk. In Section 3.3, we evaluate these numerically for a LNOI polarization rotator.

2.2. CMT-based design of the tilted segment

To analyze polarization rotation in the tilted waveguide segment, we use our coupled-mode formalism, originally developed for a curved uniaxial waveguide [6]. For simplicity, we assume that only the fundamental TE mode and the fundamental TM mode are initially excited and denote their amplitudes with a_s and a_p, respectively. Coupling to higher-order modes can be safely neglected, because generally it is heavily phase-mismatched. We consider the column vector $a \equiv (a_s, a_p)^T$, which can be loosely interpreted as a Jones vector [6]. The basis TE and TM modes are normalized so $a^\dagger a = |a_s|^2 + |a_p|^2$ equals the total power carried in the direction of propagation.

Because the angle ϕ, between the waveguide direction and its core's optic axis, is constant along the straight oblique segment, the corresponding coupled-mode equations have constant coefficients. Thus, they can be readily integrated to relate $a(L)$, the Jones vector at the end of the

Optics EXPRESS

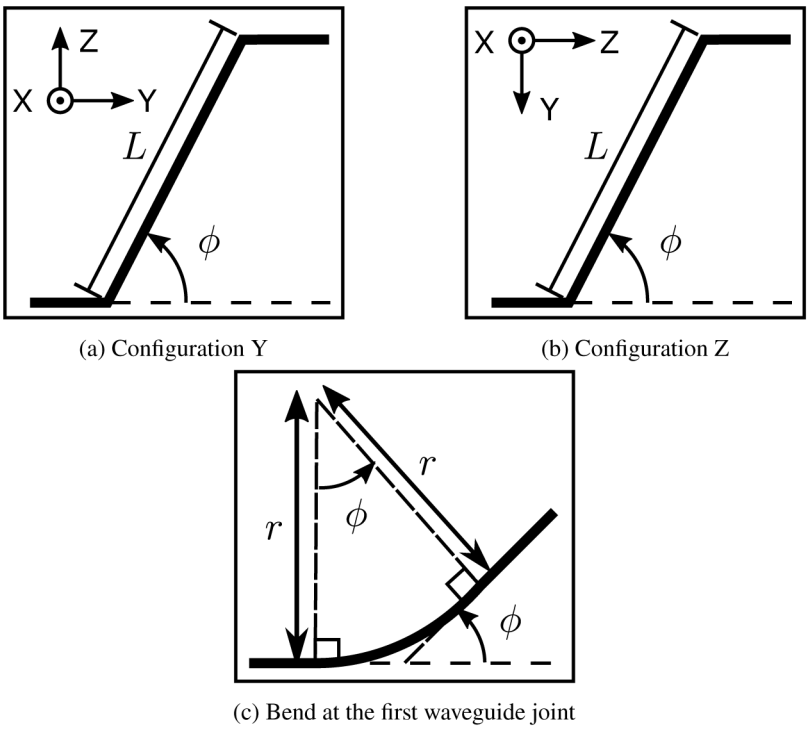

(a) Configuration Y

(b) Configuration Z

(c) Bend at the first waveguide joint

Fig. 1. (a,b) Geometry of the proposed passive polarization rotator under its two possible configurations. L is the length of the tilted segment. ϕ is the angle between the tilted segment and the corresponding LN crystallographic axis. The orientation of the crystallographic axes for each configuration is shown in the upper left corner. Light propagates from left to right. (c) Geometry of the circular bend at the first waveguide joint. r is the joint's bending radius.

oblique segment, to $a(0)$, the Jones vector at its beginning. This yields the relation

$$a(L) = \exp\left[iM(\phi)L\right] a(0). \tag{1}$$

Recall from Fig. 1 that L is the length of the oblique segment. $M(\phi)$ is a 2×2 Hermitian matrix that depends on ϕ and has the form [6]

$$M(\phi) = \begin{pmatrix} \Delta(\phi)/2 & -i\kappa(\phi) \\ i\kappa(\phi) & -\Delta(\phi)/2 \end{pmatrix}, \tag{2}$$

where $\Delta(\phi)$ and $\kappa(\phi)$ are the real-valued functions of ϕ

$$\Delta(\phi) = \Delta_0 + \Delta_1 \cos 2\phi, \quad \kappa(\phi) = \kappa_0 \sin 2\phi. \tag{3}$$

Equation (1) is analogous to that obtained for directional couplers. It shows that power is peridically exchanged between the TE and TM polarizations when $\kappa(\phi)$ is non-zero.

Physically, the functions $\Delta(\phi)$ and $\kappa(\phi)$ are, respectively, the ϕ-dependent detuning in propagation constants between the TE and TM modes; and the ϕ-dependent coupling coefficient. Correspondingly, Δ_0, Δ_1, and κ_0 are three real-valued, ϕ-independent coefficients, henceforth referred to as "polarization parameters". They represent, respectively: the direction-averaged detuning; the amplitude of oscillation in detuning with varying ϕ; and the coupling coefficient

Optics EXPRESS

when $\sin 2\phi = 1$. These parameters can be calculated in terms of the TE and TM modes' field distributions at $\phi = 0$ and their corresponding propagation constants. The required formulas were originally published in Ref. [6], but they are also reported in Appendix A. for completeness.

Given Eqs. (1) and (2), the oblique waveguide segment of length L acts as a full polarization rotator if and only if

$$\Delta(\phi) = 0, \tag{4}$$

$$L\kappa(\phi) = \pi(2n + 1)/2, \tag{5}$$

for some integer n. Equation (4) can be interpreted as requiring the TE and TM modes of the oblique waveguide to be phase-matched, and it restricts ϕ to a discrete set of values. If Eq. (4) is satisfied, then ϕ is fixed by it, and Eq. (5) becomes a constraint on L. This constraint is analogous to setting the length of a directional coupler equal to an odd-integer multiple of its minimum length for full power transfer.

As stated, Eq. (4) can only be met by a discrete set of tilt angles ϕ. For concreteness, we restrict ϕ to lie in the first quadrant, i.e. $\phi \in [0, \pi/2]$. Then ϕ satisfying Eq. (4) becomes unique and given by

$$\phi = \frac{1}{2}\text{acos}\left(-\frac{\Delta_0}{\Delta_1}\right) = \frac{\pi}{4} + \frac{1}{2}\text{asin}\left(\frac{\Delta_0}{\Delta_1}\right), \tag{6}$$

where $\text{acos}(x) \in [0, \pi]$ and $\text{asin}(x) \in [-\pi/2, \pi/2]$ for $x \in [-1, 1]$. Alternative polarization-rotator designs can be made because solutions ϕ for Eq. (4) can be found in any quadrant $[m\pi/2, (m + 1)\pi/2]$ for integer m. These alternative values are found through the transformations $\phi \to -\phi$, $\phi \to \phi - \pi$, and $\phi \to -\phi + \pi$. The first of these transformations results in a rotator with identical performance. The last two are comparatively undesirable: they only increase $|\phi|$, which leads to longer circular arcs at the joints, and, thus, larger insertion loss.

Of course, Eq. (6) yields a real-valued ϕ if and only if $|\Delta_0/\Delta_1| \leq 1$. Additionally, $|\Delta_0/\Delta_1|$ cannot be unity, because then $\kappa(\phi)$ vanishes and Eq. (5) cannot be satisfied. Hence, a necessary condition for Eqs. (4) and (5) to be satisfied simultaneously is

$$|\Delta_0/\Delta_1| < 1. \tag{7}$$

As evident from the formulas in Appendix A, the polarization parameters depend implicitly on the optical frequency and the waveguide cross-section. Hence, Eq. (7) is a necessary condition on these parameters for the waveguide segment to function as a full polarization rotator for some orientation angle ϕ.

Given Eq. (6) for ϕ, the second condition for full power transfer, i.e. Equation (5), can be satisfied if the tilted-segment length L is set equal to

$$L = \frac{\pi}{2|\kappa_{\text{eff}}|}, \quad \text{where} \quad \kappa_{\text{eff}} \equiv \kappa_0\sqrt{1 - (\Delta_0/\Delta_1)^2}. \tag{8}$$

As our notation suggests, κ_{eff} acts as the effective coupling constant along the tilted segment.

Of course, Eq. (5) is still satisfied if L is set equal to an odd-integer multiple of the right-hand side of Eq. (8). Nonetheless, just as in directional-coupler design, the smallest possible L is preferable because it results in the largest bandwidth for polarization-convertion and incurs the lowest possible material loss.

If ϕ was chosen to lie outside the first quadrant, the sign of the radical (and hence that of κ_{eff}) in Eq. (8) might change. Such change in sign does not change the power exchange between polarization modes, however.

Optics EXPRESS

2.3. Residual crosstalk due to finite curvature at the joints

Let r be the bending radius of both of the curved segments joining the tilted segment to one of the straight segments in Fig. 1. In Section 2.2, we assumed r to be small enough that polarization coupling along the curved segments is negligible. However, polarization coupling along these segments does occur, resulting in residual crosstalk X_r, i.e. a non-zero normalized power remaining in the original polarization mode after propagation along the rotator. In Appendix B, we show that, to first-order perturbation theory in $r|\kappa_0|$, X_r is given by

$$X_r = 4r^2 \left| \int_0^{\phi} \mathrm{d}\phi' \kappa(\phi') \exp\left[ir \int_0^{\phi'} \mathrm{d}\phi'' \Delta(\phi'') \right] \right|^2 . \tag{9}$$

Hence, neglect of the curved segments is accurate if $X_r \ll 1$. In deriving Eq. (9), we assume r to be common to both joints for simplicity. This simplification is sufficient because we are mostly interested in studying the effect of finite curvature on X_r, rather than the interference due to mismatch in the joints' curvatures.

The right-hand side of Eq. (9) is a complicated transcendental function of r. However, it admits a simple bound, quadratic in r, given by

$$X_r \leq (r/r_0)^2 , \quad \text{where} \quad r_0 \equiv \frac{1}{2|\kappa_0| \sin^2 \phi}. \tag{10}$$

Thus, if $r \ll r_0$, then $X_r \ll 1$. As discussed in Appendix B, the crosstalk X_r approaches its upper bound in Eq. (10) if the accumulated phase-mismatch , i.e. the argument of the exponential in Eq. (9), is negligible.

In addition to introducing polarization crosstalk, waveguide curvature at the rotator's joints induces bending losses and mode distortion [30]. Neither of these effects are modeled by our CMT description of mode coupling, as discussed in Ref. [6]. However, these effects can be inhibited in LNOI by leveraging the platform's large index contrast [5]. Nonetheless, if the bending radius r becomes comparable to the waveguide width and/or the optical wavelength, bending loss and mode distortion may become prominent [30]. Bending loss, in particular, may noticeably increase the rotator's insertion loss if r if chosen too small. Thus, there exists a trade-off between bending loss and residual polarization crosstalk one should engineer when fabricating a rotator using our proposed design.

2.4. Differences between configurations

In the framework of CMT, the difference between the two configurations of Fig. 1 lies in their respective values for the polarization parameters. Because the core's (LN's) material birefringence is small, CMT in general, and Eq. (3) in particular, are accurate for any orientation ϕ. Hence, we can estimate the polarization parameters for one configuration from those for the other by applying the shifts $\Delta(\phi) \rightarrow \Delta(\phi \pm \pi/2)$ and $\kappa(\phi) \rightarrow \kappa(\phi \pm \pi/2)$ and matching the resulting expressions to the original form, Eq. (3). Thus, to the accuracy of CMT, the polarization parameters transform as

$$\Delta_0 \rightarrow \Delta_0, \quad \Delta_1 \rightarrow -\Delta_1, \quad \kappa_0 \rightarrow -\kappa_0, \tag{11}$$

when going from Configuration Y to Configuration Z, or vice versa.

Of course, even if accurate, CMT is only approximate so Eq. (11) is not exact. Nonetheless, we have verified Eq. (11) to be accurate for small normalized material birefringence, i.e. when

$$|n_e^2 - n_o^2| \ll n_e^2 + n_o^2, \tag{12}$$

where n_e (n_o) is the core's extraordinary (ordinary) index of refraction. This is unsurprising as when Eq. (12) holds, the perturbation due to the reorientation of the permittivity dyadic is small,

Optics EXPRESS

so CMT is expected to hold. For LN at a wavelength near 1550 nm, $n_e = 2.14$ and $n_o = 2.21$ [5], so Eq. (12) is well satisfied.

Next, we examine the effect of Eq. (11) on the design of the polarization rotator. Under the transformation of Eq. (11), Eq. (8) for L remains invariant; and Eq. (6) for ϕ is reflected about $\pi/4$.

The change in ϕ makes intuitive sense, as this shift in ϕ geometrically corresponds to one of two cases. In one case, the new value for ϕ corresponds to the original orientation, measured from the new axis reference: Z instead of Y, or vice versa. In the second case, the new ϕ corresponds to a direction given by one of the quadrant transformations discussed in the paragraph following Eq. (6). Ultimately, polarization rotation along the tilted segment is unaltered by the choice of configuration.

On the other hand, the geometry of the curved joints does change between configurations. Applying Eq. (11) to Eq. (6), it follows that if $|\phi|<\pi/4$ for one configuration, we have $\pi/4<|\phi| \leq \pi/2$ for the other, and vice versa. Thus, for a fixed bending radius r, the length $r|\phi|$ spanned by each curved segment changes between configurations. For fixed r, larger $|\phi|$ implies longer propagation length and hence, larger propagation loss.

Hence, one would expect that the configuration resulting in smaller $|\phi|$ would be preferable, as it would result in smaller propagation loss and smaller crosstalk X_r due to residual polarization coupling. However, such conclusion is generally incorrect for two reasons. First, LNOI's high index-contrast enables bent waveguides with small r and low losses. Hence, propagation losses along the curved joints can be made negligible compared to those along the tilted segment, independent of the configuration. Thus, the main criterion to choose the rotator configuration should be to minimize X_r. Second, phase-mismatch between the polarization-modes along the curved segments may result in the configuration with larger $|\phi|$ having the smaller X_r. This point if further discussed in Section 3.3.

3. Numerical analysis of a LNOI rotator

In this section, we evaluate numerically the polarization parameters of a particular LNOI waveguide and examine its resulting polarization properties. The waveguide consists of a LN core with silicon-dioxide as bottom cladding and air as top cladding. We design the LNOI polarization rotator to operate at telecom wavelength, $\lambda_0 = 1550$ nm. At this wavelength, LN has the ordinary and extraordinary refractive indices of 2.21 and 2.14, respectively [5]; and silicon dioxide has a refractive index of 1.44.

For simplicity, we assume the core layer to be wide enough so its width can be taken as infinite. Hence, its height (or thickness) h is the only geometrical parameter characterizing the waveguide cross-section. This assumption facilitates numerical evaluation of the polarization parameters, while still yielding results close to those for rectangular waveguides with finite width. In Ref. [6], this approximation was examined numerically and found to be accurate for the LNOI platform. This infinite-width simplification is also consistent with the observation that waveguide width has negligible effect on polarization coupling, so long as it is larger than twice its height, as reported in Ref. [14].

For concreteness, we design the rotator using Configuration Y. As discussed in Section 2.4, the only significant difference between configurations is the residual crosstalk X_r due to finite joint curvature. X_r for both configurations is calculated and compared in Section 3.3.

3.1. Polarization parameters and tilt-segment orientation

To let our results be general, we normalize the polarization parameters by dividing them by the optical wavenumber $k_0 = 2\pi/\lambda_0$. Once normalized, these parameters depend not on the height h and the wavelength λ_0 separately, but only on the optical thickness h/λ_0. This follows from the scale invariance of Maxwell's equations [31].

Optics EXPRESS

Figure 2(a) shows the dependence of the polarization parameters on h/λ_0 in the range of 0.4–0.8. In this interval, the ratio Δ_0/Δ_1 has a magnitude of the order of unity, which allows the condition in Eq. (7) to be satisfied over an appreciable sub-interval. The coupling coefficient κ_0/k_0 varies considerably (by a factor of 6) over this range. Δ_0/k_0 decreases monotonically with optical thickness, going from 0.06 to -0.02. In contrast to these two, Δ_1/k_0 remains relatively constant around the value of -0.04.

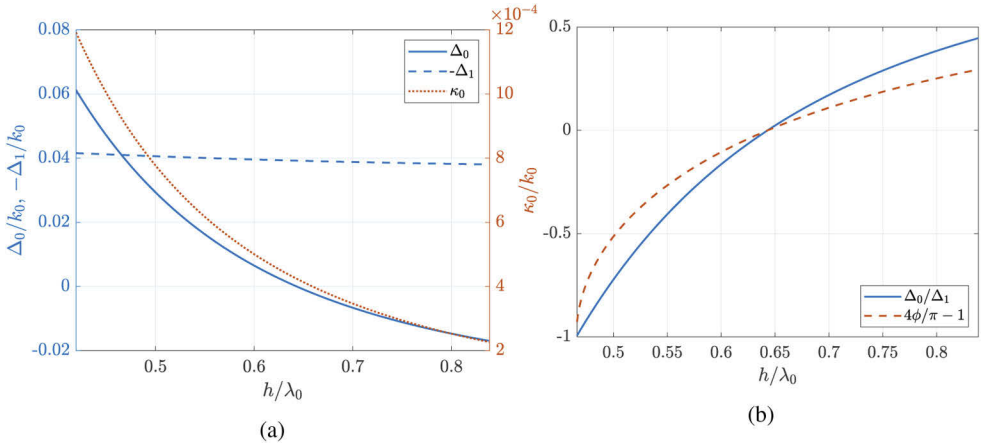

Fig. 2. (a) Polarization parameters Δ_0, Δ_1, and κ_0 as functions of optical thickness h/λ_0. The negative of Δ_1 is plotted, rather than Δ_1 directly, so the point where $\Delta_0 = -\Delta_1$ is visually evident. (b) Ratio Δ_0/Δ_1 (solid) and the angle ϕ (dashed) as functions of optical thickness h/λ_0.

We find that, over the studied h/λ_0 interval, Condition 7 is satisfied if and only if h>0.4655λ_0. This agrees with the previous observation [14] that, for a given thickness h, full mode-hybridization is possible for some waveguide orientation ϕ if and only if the wavelength λ_0 is below a threshold value. In this case, the threshold value would be that of $h/0.4655 = 2.148h$.

From the values of the polarization parameters in Fig. 2, we evaluate the parameter ratio Δ_0/Δ_1 and the concomitant tilt angle ϕ for phase-matched polarization coupling, via Eq. (6). The results are plotted in Fig. 2(b) as a function of h/λ_0, starting from the minimum value of $h/\lambda_0 = 0.4655$ necessary to satisfy Condition 7. As expected from Fig. 2(a), the curve for Δ_0/Δ_1 follows closely the shape of $-\Delta_0/k_0$ because Δ_1/k_0 remains relatively constant and negative in the considered interval for h/λ_0. As h/λ_0 increases, the monotonic increase of Δ_0/Δ_1 leads to a monotonic increment in ϕ, as follows from Eq. (6). As a consequence of the nonlinear relationship between Δ_0/Δ_1 and ϕ [Eq. (6)], the rapid increment in Δ_0/Δ_1 immediately after $h/\lambda_0 = 0.4687$ results in an even faster increase in ϕ with h/λ_0. Then, the increase in ϕ slows down as it approaches $\phi = \pi/4$, since there the derivative of ϕ with respect to Δ_0/Δ_1 reaches its minimum.

3.2. *Effective coupling coefficient and rotator bandwidth*

From Eq. (8), $|\kappa_{\text{eff}}|$ is inversely proportional to the length of the tilted segment and, thus, to the associated propagation loss in decibels. Hence, a larger $|\kappa_{\text{eff}}|$ is more desirable, as it results in a device with smaller footprint and lower insertion loss. Figure 3(a) shows the variation of $|\kappa_{\text{eff}}|/k_0$ with h/λ_0. It vanishes when $h = 0.4655\lambda_0$, where $\Delta_0 = -\Delta_1$, as a consequence of its definition, Eq. (8). Then, it rapidly increases with h/λ_0 and reaches a maximum of 5.7556×10^{-4} when $h = 0.5283\lambda_0$. Afterwards, $|\kappa_{\text{eff}}|/k_0$ decreases slowly with increasing h/λ_0 over the sampled interval. The presence of a maximum in $|\kappa_{\text{eff}}|$ can be understood from Eq. (8) as a consequence of the interplay in the dependence on h/λ_0 of its two factors: $|\kappa|$, which decreases monotonically

Optics EXPRESS

with increasing h/λ_0; and $\sqrt{1-(\Delta_0/\Delta_1)^2}$, which increases from zero at $h = 0.4655\lambda_0$, where $\Delta_0 = -\Delta_1$, as found in Fig. 2(b).

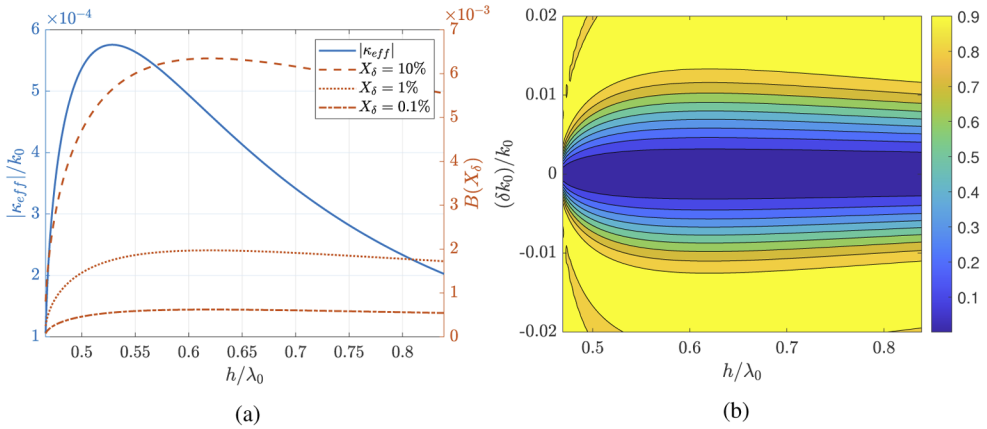

Fig. 3. (a) Effective coupling coefficient $|\kappa_{\text{eff}}|$ and normalized rotator bandwidth $B(X_\delta)$ ($X_\delta = 10\%, 1\%, 0.1\%$) as functions of optical thickness h/λ_0. (b) Contours of constant detuning-induced crosstalk X_δ as function of waveguide^\primes thickness h/λ_0 and relative detuning $\delta k_0/k_0$.

Because $|\kappa_{\text{eff}}|$ is maximized at $h = 0.5283\lambda_0$ for a given wavelength, this thickness h results in the minimum rotator length L. For example, at $\lambda_0 = 1550$ nm, the minimum-length thickness is 819 nm. From Figs. 2(b) and 3(a), the corresponding tilt angle ϕ and waveguide length L are 0.5045 radians (29 degrees) and 673 μm, respectively. LNOI waveguides with losses of 0.1 dB/cm or less can be reliably fabricated through dry-etching [5]. For a 673 μm-long polarization rotator, losses are thus estimated to be 6×10^{-3} dB or less. Even if this loss value increases to 10^{-2} dB when the waveguide thickness and other parameters do not have their optimum values, losses for our proposed polarization rotator are low enough to be acceptable for practical application.

For practical use, the bandwidth of the polarization rotator is of interest. Full polarization rotation (100% power transfer) occurs only for a target wavenumber, k_0, even when residual crosstalk X_r from Eq. (9) is negligible. When k_0 deviates from this target value, a fraction X_δ of the input power is left in the input polarization. This results in polarization crosstalk and thus limits the device's bandwidth.

To evaluate the ideal rotator's bandwidth, we evaluate X_δ directly from Eq. (1) and study it as a function of wavenumber shift, δk_0, for various rotator thicknesses. To isolate the effect of wavelength detuning, we assume r is large enough so X_r in Eq. (9) can be safely neglected. Thus, in Fig. 3(b), we report a contour-plot of X_δ as a function of h/λ_0 and the normalized wavenumber shift, $\delta k_0/k_0$. For a given optical thickness, the dependence of X_δ on detuning is easy to describe. Naturally, X_δ vanishes for $\delta k_0 = 0$. For small $|\delta k_0|/k_0$ (e.g. $|\delta k_0|/k_0 < 5\times10^{-3}$ for $h > 0.5\lambda_0$), X_δ increases quadratically with δk_0. For larger $|\delta k_0|/k_0$, X_δ begins to saturate and tends towards its maximum $X_\delta = 1$.

Next, we examine the shape of the lines of constant X_δ in Fig. 3(b). We note that they all converge at the point $h/\lambda_0 = 0.4655, \delta k_0 = 0$. Clearly, a polarization rotator with thickness $h = 0.4655\lambda_0$ has vanishing bandwidth. As h/λ_0 increases beyond this value, the contours of constant X_δ spread out rapidly until $h = 0.6196\lambda_0$, where they all reach their respective maxima in $|\delta k_0|$. Thereafter, the constant-crosstalk lines seemingly converge slowly towards a point located to the right of the sampled parameter space (large $h \gg \lambda_0$) with $\delta k_0 = 0$.

The behavior of X_δ in Fig. 3(b) suggests that any measure of the rotator's bandwidth displays a maximum around $h = 0.6196\lambda_0$. To confirm this statement, we evaluate the normalized

Optics EXPRESS

bandwidth $B(X_\delta)$, defined as a dimensionless quotient. Its numerator is the absolute difference between the detunings δk_0 of smallest magnitude resulting in a crosstalk of X_δ; its denominator, the device's nominal wavenumber k_0. We compute $B(X_\delta)$ for X_δ = 10%, 1%, and 0.1% as a function of h/λ_0 using a numerical nonlinear-equation solver. The results are shown in Fig. 3(a) with the y-scale on the right side. As expected, all three curves for $B(X_\delta)$ vanish at $h = 0.4655\lambda_0$ and peak at $h = 0.6196\lambda_0$. After the maximum, all curves feature the slow descent observed in the lines of constant X_δ of Fig. 3(b).

Analysis of the $B(X_\delta)$ curves in Fig. 3(a) allows the determination of the required rotator geometry for a given bandwidth specification. For example, if the acceptable crosstalk is −20 dB (X_δ = 1%), $B(X_\delta)$ is close to 0.2% for h>$0.55\lambda_0$. At the telecom wavelength of 1550 nm, this translates to a detuning of up to 1.5 nm on each side. If we are willing to accept a larger crosstalk of up to −10 dB (X_δ = 10%), the detuning can be as large as 4.5 nm.

3.3. *Residual crosstalk due to finite curvature at the joints*

Next, we evaluate the residual crosstalk X_r due to polarization coupling along the curved joints for the LNOI rotator. As discussed in Sec. 2.3, this is governed by Eqs. (9) and (10). First, we evaluate r_0, the upper bound on the bending radii r, defined in Eq. (10). Thus, in Fig. 4(a) we plot r_0 on a logarithmic scale as a function of h/λ_0 for both configurations, Y and Z; and label them $r_0^{(y)}$ and $r_0^{(z)}$, respectively. From Fig. 4(a), two features are most prominent. First, $r_0^{(y)}$ diverges as h/λ_0 approaches 0.4655 from the right. Second, $r_0^{(y)}$>$r_0^{(z)}$ if h<$0.6667\lambda_0$ and $r_0^{(0)}$<$r_0^{(e)}$ if h>$0.6667\lambda_0$.

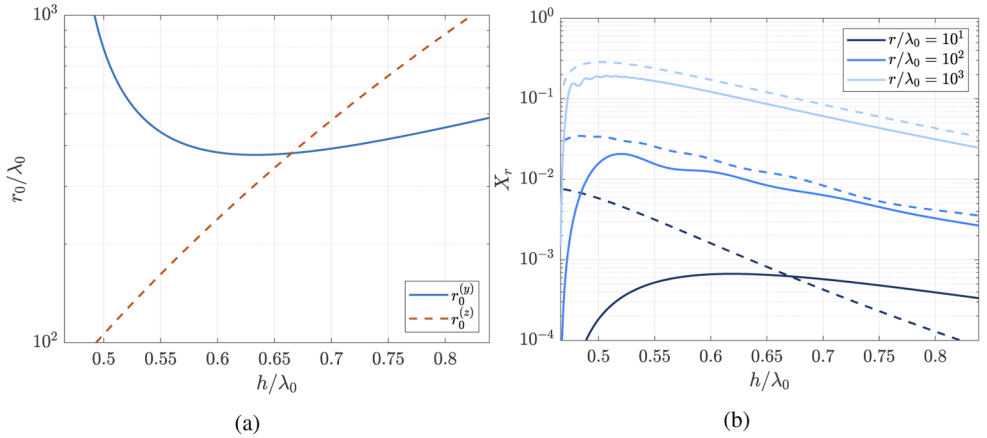

Fig. 4. (a) Bound r_0 on the bending radius r as a function of optical thickness h/λ_0. r_0 is such that $r \ll r_0$ ensures negligible polarization coupling along the curved joints. $r_0^{(y)}$ ($r_0^{(z)}$) is r_0 for Configuration Y (Configuration Z). (b) Residual crosstalk X_r as a function of optical thickness h/λ_0, calculated for different bending radii ($r/\lambda_0 = 10^1, 10^2, 10^3$). Solid lines correspond to Configuration Y; dashed lines, to Configuration Z.

These two features can be understood from the definition of r_0, Eq. (10). The divergence of $r_0^{(y)}$ is a consequence of the facts that r_0 is inversely proportional to $\sin^2\phi$ and that ϕ vanishes at $h = 0.4655\lambda_0$, as seen in Fig. 2(b). Meanwhile, the crossing of $r_0^{(y)}$ and $r_0^{(z)}$ at $h = 0.6667\lambda_0$ occurs because, in this neighborhood of h/λ_0, Δ_0 vanishes, as seen in Fig. 2(a). Consequently, $\phi = \pi/4$ for both configurations, according to Eqs. (6) and (11). Because $|\kappa|$ is (approximately) invariant between configurations, Eq. (10) then yields identical expressions for r_0 for both configurations when $\phi = \pi/4$. We acknowledge that this argument is not exact, as $r_0^{(o)}$ and $r_0^{(e)}$ in Fig. 4(a)

Optics EXPRESS

intersect at $h = 0.6667\lambda_0$, but Δ_0 vanishes for Configuration Y at $h = 0.6427\lambda_0$, as seen in Fig. 2. However, we attribute this slight discrepancy to the approximate (rather than exact) nature of CMT, as discussed in Sec. 2.4.

These features of Fig. 4(a) suggest that, to minimize X_r, one should use Configuration Y if $h<0.6667\lambda_0$ and Configuration Z if $h>0.6667\lambda_0$, regardless of r. However, to achieve a stronger conclusion, we must examine the transcendental expression for X_r in Eq. (9), rather than just its simpler bound, Eq. (10). Thus, we evaluate X_r from Eq. (9) numerically for both configurations, for a continuum of values of h/λ_0, and for discrete values of r/λ_0; specifically, $r/\lambda_0 = 10^1, 10^2, 10^3$. The results are plotted on a logarithmic scale in Fig. 4(b).

For $r/\lambda_0 = 10$, the curve for X_r in Fig. 4(b) is well described as that of r_0/λ_0 in Fig. 4(a), albeit subjected to a vertical stretch and a reflection over the y-axis. This implies that X_r is well approximated by the upper bound 10. This is expected, because for sufficiently small r (lower than or of the order of $|\Delta_1|^{-1}$), the phase factor in the integrand of Eq. (9) approximates unity, and Eq. (10) becomes an equality for X_r.

For larger values of r ($r \gg |\Delta_1|^{-1}$), however, the phase factor in Eq. (9) oscillates rapidly with the integrand. Consequently, X_r becomes much smaller than its upper bound of r/r_0. Of course, the effect is more noticeable for larger ϕ, as then the phase of the integrand in Eq. (9) oscillates more over the integration domain. To see this, compare the curves for $r/\lambda_0 = 10^2$ and $r/\lambda_0 = 10^3$ with those for $r/\lambda_0 = 10^1$. If the integrand still oscillated slowly in phase, the $r/\lambda_0 = 10^2$ and $r/\lambda_0 = 10^3$ would be identical to those for $r/\lambda_0 = 10^1$, merely shifted along the logarithmic y-axis by factors of 10^2 and 10^4, respectively. However, the $r/\lambda_0 = 10^2$ and $r/\lambda_0 = 10^3$ curves are noticeably below those predicted through these shifts to the $r/\lambda_0 = 10^1$ lines, as expected.

Additionally, we observe that the $r/\lambda_0 = 10^2$ and $r/\lambda_0 = 10^3$ curves get closer to their corresponding $r/\lambda_0 = 10^1$ lines, the larger tilt angle ϕ is. Specifically, for Configuration Y, the $r/\lambda_0 = 10^2$ and $r/\lambda_0 = 10^3$ lines grow closer to the $r/\lambda_0 = 10^1$ line as h/λ_0 increases, because ϕ increases with h/λ_0, as seen in Fig. 2(b). For Configuration Z, the $r/\lambda_0 = 10^2$ and $r/\lambda_0 = 10^3$ curves grow closer to $r/\lambda_0 = 10^1$ curve as h/λ_0 decreases. This is because ϕ increases with decreasing h/λ_0 in this configuration, by applying the arguments of Sec. 2.4 to ϕ in Fig. 2(b). This agrees with our claim that larger ϕ leads to larger inhibition of X_r due to phase-mismatch.

The net effect is that Configuration Y yields a smaller residual crosstalk X_r at any waveguide thickness, for $r/\lambda_0 = 10^2$ and $r/\lambda_0 = 10^3$. This is because, at small h/λ_0, its upper bound of r/r_0 tends to zero as $\phi \to 0$; and, for large h/λ_0, the larger ϕ leads to a larger accumulated phase-mismatch. Only for small r ($r/\lambda_0 \approx 10^1$), phase-mismatch is small overall and the conclusion from Fig. 4(a) holds, which recommends Configuration Z for large h/λ_0 ($h>0.6667\lambda_0$).

4. Conclusion

We utilized our recently developed couple-mode theory to design a passive polarization rotator, coupling fundamental polarization modes. It consists of a LNOI waveguide tilted at an optimum angle, such that material anisotropy induces phase-matched polarization coupling. We discussed how the device's tilt angle and length depend on the core's thickness h and the incident wavelength λ_0 through the optical thickness h/λ_0. We discussed two sources of crosstalk: the finite curvature of the waveguide joints, and wavelength detuning from the device's nominal wavelength. From this discussion, we showed that joint-curvature crosstalk is negligible for experimentally feasible bending radii, and we characterized the crosstalk-limited bandwidth of the device. Our results suggest that compact (length <1 mm), low-loss, passive polarization rotators can be fabricated with our proposed design.

Appendix A: formulas for the polarization parameters

In this appendix, we provide explicit formulas for the polarization parameters Δ_0, Δ_1 and κ_0 in terms of the normal modes of a $LiNbO_3$ waveguide, for which the direction of propagation is

Optics EXPRESS

either parallel or perpendicular to the optic axis ($\phi = 0$). These are derived in Ref. [6] and are given by

$$\Delta_0 = \beta_s - \beta_p - \Delta_1, \quad \Delta_1 = \xi\left(K_{ss}^{(1)} + K_{pp}^{(3)}\right), \quad \kappa_0 = -\xi\Im K_{sp}^{(2)}. \tag{13}$$

In Eq. (13), β_s and β_p are, respectively, the propagation constants of the TE and TM modes at $\phi = 0$. The parameter ξ is a dimensionless measure of the uniaxial core's material birefringence. In terms of the material's extraordinary refractive index n_e and ordinary index n_o, ξ is defined as the ratio

$$\xi \equiv \pm(n_e^2 - n_o^2)/(n_e^2 + n_o^2), \tag{14}$$

where the positive (negative) sign is taken when the direction of propagation is parallel (perpendicular) to the optic axis at $\phi = 0$.

In Eq. (13), $K_{ss}^{(1)}$, $K_{sp}^{(2)}$, and $K_{pp}^{(3)}$ are overlap integrals with units of reciprocal length. To write explicit formulas for them, we use a Cartesian coordinate system $\{\hat{\mathbf{x}}, \hat{\mathbf{y}}, \hat{\mathbf{z}}\}$ such that $\hat{\mathbf{z}}$ is the direction of propagation, $\hat{\mathbf{x}}$ lies in the plane of propagation; and $\hat{\mathbf{y}}$ is normal to this plane. The three axes are orientated such that the direction of positive $\hat{\mathbf{y}}$ points towards the waveguide's upper cladding.

Let E_{xs} and E_{xp} be the x component of the electric field for the TE and TM modes, respectively. Introducing the transverse part of the magnetic fields for these two modes (i.e., $\mathbf{H}_{ts} \equiv \mathbf{H}_s - \hat{\mathbf{z}}(\hat{\mathbf{z}}\cdot\mathbf{H}_s)$]), the overlap integrals can be written as

$$\begin{aligned} K_{ss}^{(1)} &= \frac{\bar{\epsilon}k_0\eta_0}{4}\iint_C \mathrm{d}x\mathrm{d}y\,|E_{xs}|^2\,, \\ K_{sp}^{(2)} &= \frac{i}{4}\iint_C \mathrm{d}x\mathrm{d}y\left[\mathbf{z}\cdot\left(\nabla_t\times\mathbf{H}_{ts}^*\right)E_{xp} - E_{xs}^*\mathbf{z}\cdot\left(\nabla_t\times\mathbf{H}_{tp}\right)\right], \\ K_{pp}^{(3)} &= \frac{1}{4\bar{\epsilon}k_0\eta_0}\iint_C \mathrm{d}x\mathrm{d}y\left|\nabla_t\times\mathbf{H}_{tp}\right|^2. \end{aligned} \tag{15}$$

In Eq. (15), $k_0 = \omega/c$; ω is the mode's angular frequency; c, the speed of light in vacuum; η_0, the impedance of vacuum; C, the waveguide's cross-section area; and $\nabla_t\times$, the transverse curl operator [32]. $\bar{\epsilon} \equiv (n_e^2 + n_o^2)/2$ can be interpreted as the core's permittivity, averaged over the plane of propagation. In writing Eq. (15), we assume that the modes are normalized to carry unit power, as conventional in CMT.

The term $(\nabla_t\times\mathbf{H}_t)$ in Eq. (15) can be interpreted in terms of the longitudinal component of the displacement field D_z. This follows immediately from the relation

$$\nabla_t\times\mathbf{H}_t = -i\omega D_z\mathbf{z}, \tag{16}$$

obtained from projecting Ampere's law along the $\hat{\mathbf{z}}$ axis. Substituting Eq. (16) into Eq. (15), one gets

$$\begin{aligned} K_{sp}^{(2)} &= -\frac{ck_0}{4}\iint_C \mathrm{d}x\mathrm{d}y\left(D_{zs}^*E_{xp} + E_{xs}^*D_{zp}\right), \\ K_{pp}^{(3)} &= \frac{ck_0}{4\epsilon_0\bar{\epsilon}}\iint_C \mathrm{d}x\mathrm{d}y\left|D_{zp}\right|^2. \end{aligned} \tag{17}$$

The combination of Eqs. (13) and (17) shows that power exchange between the s and p modes (due to κ_0) arises from the coupling between the longitudinal displacement field D_z and the transverse electric field E_x of orthogonally polarization modes. It is important to remember that the D_z in Eq. (17) follows from Eq. (16). It is related to the electric field of the corresponding mode through the permittivity dyadic of the untilted ($\phi = 0$) waveguide, rather than that of the tilted segment.

As in Sec. 3., it is often convenient to consider the idealized case where the waveguide cross-section is infinitely large along one transversal direction. We found in Ref. [6] that

Optics EXPRESS

polarization coupling vanishes if the infinitely extended direction is along y, but not if it is along x. Thus, we need consider only the latter case. In that situation, two changes to Eqs. (15) and (17) must be made. First, the integrals over x and y become only over the y coordinate of the core. Second, the TE and TM modes are normalized to carry unit power per length along x, rather than unit power when integrated over both transverse dimensions.

Appendix B: crosstalk due to polarization coupling along the curved joints

Consider the joints at the beginning and both ends of the tilted segment of the polarization rotator in 1. To minimize propagation losses, each consists of a circular arc of radius with a central angle equal to the tilt angle ϕ. In the polarization rotator design of Sec. 2.2, we assume these circular arcs are short enough so polarization coupling along them is negligible. Nonetheless, because of their finite size, polarization coupling does occur along them, resulting in a small fraction of power remaining in the original polarization, i.e. crosstalk. In this appendix, we derive a perturbative expression and bound for this crosstalk.

To do so, we first need a general relation between the propagation coordinate z (not to be confused with the crystallographic Z-axis of LN) and the local tilt angle χ of the waveguide, that accounts for the curved joints. The simplest relation of this sort is given by

$$\chi(z) = \begin{cases} (z - z_0)/r, & z_0 \le z < z_1, \\ \phi, & z_1 \le z < z_2, \\ (z_3 - z)/r, & z_2 \le z \le z_3, \end{cases} \tag{18}$$

where r is the radius of curvature common to both joints and the discrete lengths points z_n are

$$z_0 = -r\phi, \quad z_1 = 0, \quad z_2 = L, \quad z_3 = L + r\phi, \tag{19}$$

where, as in the main text, L and ϕ are the length and tilt angle of the oblique waveguide segment, respectively.

As stated in Section 3.3, we are mostly interested in the effect of nonzero bending radii, and not so much in the interference due to mismatch in their values. Hence, we take r as common to both joints in Eq. (18), for simplicity. It is straightforward to generalize the subsequent analysis to distinct bending radii.

Next, we consider the propagation matrix $U(z_3, z_0)$, defined as the 2×2 matrix relating the Jones vector $a(z_3)$ at the endpoint z_3 to $a(z_0)$ at the initial point z_0. It is analogous to the time-evolution operator from quantum mechanics [6,33]. Given its composition property [33], $U(z_3, z_0)$ can be evaluated as the product

$$U(z_3, z_0) = U(z_3, z_2)U(z_2, z_1)U(z_1, z_0). \tag{20}$$

Next, we evaluate each propagation matrix in the right-hand side of Eq. (20) to find an explicit expression for the net propagation matrix $U(z_3, z_0)$.

We assume that the tilted segment is designed according to Sec. 2.2; i.e. with its tilt angle ϕ given by Eq. (6), and its length L given by Eq. (8). Then,

$$U(z_2, z_1) = \exp[iM(\phi)L] = i\mathrm{sgn}(\kappa_{\mathrm{eff}})\sigma_3 \tag{21}$$

where $\mathrm{sgn}(\cdot)$ is the signum function, and σ_n ($n = 1, 2, 3$) represent the Pauli matrices, defined as

$$\sigma_1 \equiv \begin{pmatrix} 1 & 0 \\ 0 & -1 \end{pmatrix}, \quad \sigma_2 \equiv \begin{pmatrix} 0 & 1 \\ 1 & 0 \end{pmatrix}, \quad \sigma_3 \equiv \begin{pmatrix} 0 & -i \\ i & 0 \end{pmatrix}. \tag{22}$$

The Pauli matrices are labeled following optics convention [6,34], so that the Stokes parameters S_n of the Jones vector a are given by $S_n = a^\dagger \sigma_n a$ ($n = 1$–3).

Optics EXPRESS

Next, we evaluate $U(z_1, z_0)$ and $U(z_3, z_2)$. They are solutions to the differential equation [6]

$$i\frac{\mathrm{dv}}{z}U(z, z_n) = M\left[\chi(z)\right]U(z, z_n), \quad (n = 0, 2) \tag{23}$$

for $z \in (z_n, z_{n+1})$, along with the initial condition

$$U(z_n, z_n) = I, \tag{24}$$

where I is the 2×2 identity matrix.

Equations (23) and (24) do not admit general closed-form solutions, so we solve them approximately via perturbation theory. To do so, we express $M(\chi)$ as the sum of two parts: one modeling the χ-dependent effective-index detuning between the polarization modes, and one modeling the χ-dependent coupling strength. Thus, using the Pauli matrices σ_n, we write

$$M(\chi) = \frac{1}{2}\Delta(\chi)\sigma_1 + \kappa(\chi)\sigma_3. \tag{25}$$

We assume

$$|\kappa_0|(z_{n+1} - z_n) \ll 1, \quad (n = 0, 2) \tag{26}$$

so the second term in the right side of Eq. (25) makes only a perturbative contribution to the polarization dynamics along the curved joints. Then, the corresponding $U(z_{n+1}, z_n)$ matrices have a rapidly converging Dyson series in $\kappa(\chi)$ [33].

Thus, we truncate these series after their second term to obtain the approximations

$$U(z_{n+1}, z_n) \approx U^{(0)}(z_{n+1}, z_n) + U^{(1)}(z_{n+1}, z_n), \quad (n = 0, 2) \tag{27}$$

where $U^{(0)}(z_{2n+1}, z_{2n})$ is the zeroth-order term

$$U^{(0)}(z_{n+1}, z_n) = \exp\left\{\frac{1}{2}i\sigma_1\int_{z_n}^{z_{n+1}}\mathrm{d}z\Delta[\chi(z)]\right\}, \tag{28}$$

and $U^{(1)}(z_{2n+1}, z_{2n})$ is the first-order correction

$$U^{(1)}(z_{n+1}, z_n) = i\int_{z_n}^{z_{n+1}}\mathrm{d}zU^{(0)}(z_{n+1}, z)\kappa[\chi(z)]\sigma_3U^{(0)}(z, z_n). \tag{29}$$

We note that, although Condition 26 is sufficient for Eq. (27) to hold, it is not necessary, as the non-vanishing mismatch $\Delta(\chi)$ for $\chi \in (0, \phi)$ further inhibits coupling along the bends.

Given Eqs. (21) and (27) for the propagation matrices $U(z_{n+1}, z_n)$, we may directly evaluate Eq. (20) for $U(z_3, z_0)$ and thus the crosstalk X_r due to finite joint curvature. Let $a_s \equiv (1, 0)^T$, then one finds that X_r is given by

$$X_r = \left|a_s^\dagger U(z_3, z_0)a_s\right|^2 = 4r^2\left|\int_0^\phi \mathrm{d}\chi\kappa(\chi)\exp\left[i\theta_r(\chi)\right]\right|^2, \tag{30}$$

where $\theta_r(\chi)$ is the accumulated phase-mismatch

$$\theta_r(\chi) \equiv r\int_0^\chi \mathrm{d}\chi'\Delta(\chi'). \tag{31}$$

Clearly, Eqs. (30) and (31) together are equivalent to Eq. (9).

Because of the dependence of $\theta_r(\chi)$ on r, the right-hand side of Eq. (30) is a transcendental function of r. For a given waveguide cross-section and bending radius, the right-hand side of

Optics EXPRESS

Eq. (30) can be evaluated numerically for X_r. However, it is useful to have a simpler expression for a quick estimation of X_r. Such an expression can be obtained by noting that

$$\left|\int_0^{\phi} \mathrm{d}\chi \kappa(\chi) \exp\left[i\theta_r(\chi)\right]\right| \leq \mathrm{sgn}(\phi) \int_0^{\phi} \mathrm{d}\chi \left|\kappa(\chi) \exp\left[i\theta_r(\chi)\right]\right| = \mathrm{sgn}(\phi) \int_0^{\phi} \mathrm{d}\chi \left|\kappa(\chi)\right|. \quad (32)$$

The inequality in Eq. (32) is a well known property of complex-valued integrals [35]. Physically, the right-most side of Eq. (32) can be interpreted as the magnitude of the coupled amplitude to first-order perturbation, when phase-mismatch between the polarization modes is neglected.

To compute the integral in Eq. (32), we take ϕ to lie in either the first or fourth quadrant, so the bending segment spans the smallest possible arc. Then, combining Eqs. (30) and (32), we find the bound for X_r:

$$X_r \leq 4r^2 |\kappa_0|^2 \sin^4 \phi \quad (33)$$

Evidently, Eq. (33) is equivalent to Eq. (10). As noted for Eq. (32), X_r approaches the right-hand side of 33 when the accumulated phase-mismatch $\theta_r(\chi)$ [Eq. (31)] is negligible (i.e. $|\theta_r(\chi)| \ll \pi$) for $\chi \in (0, \phi)$.

Funding. National Science Foundation (ECCS-1807735); Consejo Nacional de Ciencia y Tecnología (2018-000009-01EXTF-00485).

Disclosures. The authors declare no conflicts of interest.

Data availability. No data were generated or analyzed in the presented research.

References

1. M. Zhang, C. Wang, R. Cheng, A. Shams-Ansari, and M. Lončar, "Monolithic ultra-high-Q lithium niobate microring resonator," Optica **4**(12), 1536–1537 (2017).
2. A. Rao and S. Fathpour, "Heterogeneous thin-film lithium niobate integrated photonics for electrooptics and nonlinear optics," IEEE J. Sel. Top. Quantum Electron. **24**, 1–12 (2018).
3. Y. He, H. Liang, R. Luo, M. Li, and Q. Lin, "Dispersion engineered high quality lithium niobate microring resonators," Opt. Express **26**(13), 16315–16322 (2018).
4. C. Wang, M. Zhang, M. Yu, R. Zhu, H. Hu, and M. Lončar, "Monolithic lithium niobate photonic circuits for Kerr frequency comb generation and modulation," Nat. Commun. **10**, 1–6 (2019).
5. D. Zhu, L. Shao, M. Yu, R. Cheng, B. Desiatov, C. Xin, Y. Hu, J. Holzgrafe, S. Ghosh, A. Shams-Ansari, E. Puma, N. Sinclair, C. Reimer, M. Zhang, and M. Lončar, "Integrated photonics on thin-film lithium niobate," Adv. Opt. Photonics **13**(2), 242–352 (2021).
6. L. Cortes-Herrera, X. He, J. Cardenas, and G. P. Agrawal, "Coupled-mode theory of the polarization dynamics inside a microring resonator with a uniaxial core," Phys. Rev. A **103**(6), 063517 (2021).
7. D. W. Berreman, "Optics in stratified and anisotropic media: 4× 4-matrix formulation," J. Opt. Soc. Am. **62**(4), 502–510 (1972).
8. D. Gia Russo and J. Harris, "Wave propagation in anisotropic thin-film optical waveguides," J. Opt. Soc. Am. **63**(2), 138–145 (1973).
9. W. Burns and J. Warner, "Mode dispersion in uniaxial optical waveguides," J. Opt. Soc. Am. **64**(4), 441–446 (1974).
10. D. Marcuse and I. Kaminow, "Modes of a symmetric slab optical waveguide in birefringent media-part ii: Slab with coplanar optical axis," IEEE J. Quantum Electron. **15**(2), 92–101 (1979).
11. A. Knoesen, T. K. Gaylord, and M. Moharam, "Hybrid guided modes in uniaxial dielectric planar waveguides," J. Lightwave Technol. **6**(6), 1083–1104 (1988).
12. A. Pan, C. Hu, C. Zeng, and J. Xia, "Fundamental mode hybridization in a thin film lithium niobate ridge waveguide," Opt. Express **27**(24), 35659–35669 (2019).
13. A. Kaushalram, G. Hegde, and S. Talabattula, "Mode hybridization analysis in thin film lithium niobate strip multimode waveguides," Sci. Rep. **10**(1), 16692–13 (2020).
14. J. Wang, P. Chen, D. Dai, and L. Liu, "Polarization coupling of x-cut thin film lithium niobate based waveguides," IEEE Photonics J. **12**(6), 1–12 (2020).
15. E. Saitoh, Y. Kawaguchi, K. Saitoh, and M. Koshiba, "TE/TM-pass polarizer based on lithium niobate on insulator ridge waveguide," IEEE Photonics J. **5**(2), 6600610 (2013).
16. Y. Liu, X. Huang, Z. Li, Y. Kuang, H. Guan, Q. Wei, Z. Fan, and Z. Li, "TE/TM-pass polarizers based on lateral leakage in a thin film lithium niobate–silicon nitride hybrid platform," Opt. Lett. **45**(17), 4915–4918 (2020).
17. Z. Gong, R. Yin, W. Ji, J. Wang, C. Wu, X. Li, and S. Zhang, "Optimal design of dc-based polarization beam splitter in lithium niobate on insulator," Opt. Commun. **396**, 23–27 (2017).
18. H. Xu, D. Dai, L. Liu, and Y. Shi, "Proposal for an ultra-broadband polarization beam splitter using an anisotropy-engineered Mach-Zehnder interferometer on the x-cut lithium-niobate-on-insulator," Opt. Express **28**(8), 10899–10908 (2020).

Optics EXPRESS

19. L. Zhang, X. Fu, and L. Yang, "Compact, broadband and low-loss polarization beam splitter on lithium-niobate-on-insulator using a silicon nanowire assisted waveguide," IEEE Photonics J. **12**(6), 1 (2020).
20. J. Schollhammer, M. A. Baghban, and K. Gallo, "Modal birefringence-free lithium niobate waveguides," Opt. Lett. **42**(18), 3578–3581 (2017).
21. A. Kaushalram and S. Talabattula, "Zero-birefringence dual mode waveguides and polarization-independent two-mode (de) multiplexer on thin film lithium niobate," Opt. Commun. **500**, 127334 (2021).
22. G. Yang, A. V. Sergienko, and A. Ndao, "Tunable polarization mode conversion using thin-film lithium niobate ridge waveguide," Opt. Express **29**(12), 18565–18571 (2021).
23. T.-J. Wang and Y.-C. Cheng, "Integrated-optic polarization rotator with obliquely deposited columnar thin film," Opt. Express **20**(1), 601–606 (2012).
24. A. Donaldson and K. Wong, "Phase-matched mode convertor in $LiNbO_3$ using near-Z-axis propagation," Electron. Lett. **23**(25), 1378–1379 (1987).
25. J. Čtyrokỳ, "Analysis of polarization effects in near-Z-axis Ti: $LiNbO_3$ devices," J. Opt. Commun. **14**, 32–38 (1993).
26. S. Bhandare, R. Noé, and D. Sandel, "Origin of reciprocal circular birefringence observed in X-cut, Z-propagation $LiNbO_3$ polarization transformers," Appl. Phys. B **73**(5-6), 549–553 (2001).
27. J. D. Bull and N. A. Jaeger, "Parasitic mode conversion in Z-propagating lithium-niobate waveguides," J. Lightwave Technol. **25**(1), 387–393 (2007).
28. D. Marcuse, "Coupled-mode theory for anisotropic optical waveguides," The Bell Syst. Tech. J. **54**(6), 985–995 (1975).
29. A. V. Tsarev, "New compact polarization rotator in anisotropic $LiNbO_3$ graded-index waveguide," Opt. Express **16**(3), 1653–1658 (2008).
30. C. Vassallo, Optical waveguide concepts, Optical wave sciences and technology (Elsevier, 1991), pp. 228–231.
31. J. D. Joannopoulos, S. G. Johnson, J. N. Winn, and R. D. Meade, Photonic crystals: molding the flow of light (Princeton University Press, 2008), 2nd ed., pp. 20–21.
32. D. Marcuse, Theory of dielectric optical waveguides, Quantum electronics–principles and applications (Academic Press, 1974), pp. 98–99.
33. A. Messiah, Quantum mechanics (North-Holland Pub. Co, 1961), Chap. XVII.
34. J. N. Damask, Polarization optics in telecommunications (Springer, 2005), pp. 54–55.
35. J. W. Brown and R. V. Churchill, Complex variables and applications, Brown-Churchill series (McGraw-Hill Higher Education, 2004), 7th ed., pp. 114-115.